Biomechan Model Mechanobiol (2007) 6:409–421
DOI 10.1007/s10237-006-0067-5

ORIGINAL PAPER

# Characterizing intramural stress and inflammation in hypertensive arterial bifurcations

**Peter H. Carnell · Raymond P. Vito · W. Robert Taylor**

Received: 4 May 2005 / Accepted: 28 November 2006 / Published online: 22 December 2006


**Abstract** A histology-based methodology was developed and used to determine whether intramural stress and combined monocyte/macrophage density positively correlate within hypertensive bifurcations. Hypertension was induced in Sprague–Dawley rats using Angiotensin II pumps. Analysis focused on mesenteric bifurcations harvested 7 days ($n = 4$) post implant, but also included normotensive ($n = 2$) and 21-day hypertensive ($n = 1$) samples. Mesentery was processed in a manner that preserves morphology, corrects for histology-related distortions and results in reconstructions suitable for finite element analysis. Peaks in intramural stress and monocyte/macrophage density occurred near bifurcations after the onset of hypertension. Cell density peaks occurred in regions where surface curvature is complex and tends to heighten intramural stress. Also, a strong positive correlation between mean stress and mean cell density suggests that they are related phenomena. A point-by-point comparison of stress and cell density throughout each bifurcation did not exhibit a consistent pattern. We offer reasons why this most stringent test did not corroborate our other findings that high intramural stress is correlated with increased inflammation near the center of the bifurcation.

P. H. Carnell (✉) · R. P. Vito
Woodruff School of Mechanical Engineering,
Georgia Institute of Technology, Atlanta, GA 30332, USA
e-mail: peter.carnell@me.gatech.edu

W. Robert Taylor
Cardiology Division, Emory University School of Medicine,
Atlanta, GA 30322, USA

W. Robert Taylor
Atlanta VA Medical Center, Decatur, GA 30032, USA

## 1 Introduction

Hypertension is a major risk factor for atherosclerosis, stroke and kidney disease (Wilson 1994; NHLBI 2003; AHA 2005). Many studies suggest that elevated intramural stresses caused by hypertension may stimulate inflammatory changes (Ollerenshaw et al. 1988; Capers et al. 1997; Glagov et al. 1997; Xu et al. 2000), but little has been done to ascertain whether inflammation and stress are spatially correlated in vivo. Establishing such correlations may help identify mechanisms that relate hypertension to adaptive and maladaptive changes in arteries. Arterial bifurcations exhibit large variations in intramural stress and are focal points for the onset of disease (Willis 1954; Thubrikar et al. 1990; Salazar et al. 1995; Thubrikar and Robicsek 1995). Hence bifurcations are a logical place to examine whether high stresses spatially correlate with the inflammation that occurs during the onset of hypertension.

We hypothesize that intramural stresses and inflammation are both elevated where arteries branch. We further hypothesize that elevated stresses in hypertensive bifurcations are correlated with increased inflammation. To examine these hypotheses we (1) developed a method that uses histological sections to reconstruct small arterial bifurcations; (2) used finite element analysis to evaluate intramural stresses; (3) quantified biological measures of inflammation; and (4) visually and statistically compared the distributions of stress and inflammation.

Chronic hypertension produces an inflammatory response characterized by the recruitment of monocytes and their differentiation into macrophages. A detailed understanding of such processes is needed to describe the mechanisms that link mechanical loads to

inflammation. However, a variety of experiments indicate that mechanical loads and inflammation are related phenomena. Howard et al. (1997) observed that cyclic stretch induced an oxidative stress in endothelial cell monolayers. Aortic coarctation studies in rats revealed that medial thickening and hypertrophy were significant in the high pressure region above the ligature but not below. The lack of cellular or structural changes below the site of coarctation suggests that downstream humoral factors did not significantly affect the morphology (Ollerenshaw et al. 1988). Moreover, a finite element study of the human carotid bifurcation suggests that stress peaks occur in regions susceptible to atherosclerotic lesions (Salazar et al. 1995). Taken together, in vitro experiments, in vivo experiments and analytical models suggest that mechanical forces and inflammation are related phenomena.

Arteries are sensitive to chronic increases in pressure and adapt in a manner that limits the levels of circumferential stress. Cell cultures of smooth muscle cells exposed to stretch can lose their contractile phenotype and tend to grow, proliferate and migrate (Griendling and Alexander 1998). The media can also exhibit considerable thickening and increased collagen synthesis when blood pressure increases (Wolinsky and Glagov 1964; Glagov et al. 1997; Xu et al. 2000). Although these examples help illustrate a relationship between form and mechanical function, they do not indicate how a chronic increase in blood pressure affects arterial bifurcations. This gap in research represents a significant void because intramural stresses vary greatly where arteries branch and bifurcations are common sites of disease.

## 2 Materials and methods

Figure 1 is a flowchart showing the methods used to characterize inflammation and stress. The quantification of cell density and stress were treated as parallel and independent tasks because a much higher image resolution was needed to identify inflammatory cells than to identify vascular structures for reconstruction. Ultimately, the stress and inflammation data were integrated through visual and statistical comparisons (Carnell 2004).

### 2.1 Animal preparation

Male Harlan Sprague–Dawley rats, aged 7–9 weeks received Angiotensin II infusion from implanted osmotic mini-pumps (75 mg/kg/day) and blood pressure was measured with a tail cuff. The rats were euthanized by $CO_2$ narcosis after 7 or 21 days. Normotensive rats were included as controls. Data suggest that macrophage migration, MCP-1 expression and SMC hypertrophy were manifest by day 7 (Fukui et al. 1997). A second, longer exposure time of 21 days was considered, since adaptive changes would be more fully expressed at this time. Mesenteric arteries were used since they contain many branches and are responsive to changes in pressure. The mesentery was pressure fixed in situ at 80 mmHg for 1 h, before being harvested, processed, and embedded in glycol methacrylate resin (GMA). For each rat a single mesenteric bifurcation was studied, including 7-day hypertensive bifurcations ($n = 4$), 21-day hypertensive bifurcations ($n = 1$) and normotensive bifurcations ($n = 2$).

### 2.2 Histology

Polysciences ImmunoBed Kit (Polysciences, Warrington, PA, Cat.# 17324) was used for embedding. Since there are numerous branches in the mesentery and several blocks can be cast from a single animal, obtaining a series of sections necessary to complete a reconstruction was possible, even when the location of a specific bifurcation could not be identified a priori. A fixture was designed to hold an array of four pins in place while the GMA polymerized (Carnell 2004). After the resin cured, the fixture and pins were removed, leaving the array of holes. Such holes would be lost in paraffin or methyl methacrylate (MMA) sections, since these media must be removed prior to staining.

The embedded specimen was mounted on a rectangular Lexan block that could be more rigidly held by a standard specimen clamp in a Microm HM 355S Rotary Microtome. Sections were cut using a motorized stroke with a tungsten carbide blade and then floated for approximately one minute on a room temperature deionized water bath. This approach tended to minimize deformations and reduce the variability from section to section.

To identify vessel structures and inflammatory cells, the sections were stained using a modified hematoxylin and eosin (H&E) protocol. Important modifications included using an aqueous-based Gill's hematoxylin, limiting exposure time to acid alcohol, and reducing the number of transitions between water and alcohol. It was found that mixtures of water and alcohol tended to partially dissolve the GMA matrix and caused some sections to partially detach from the slide. Therefore, with the exception of a 3 s exposure to acid alcohol, aqueous-based reagents were used and the sections were air-dried before and after staining. The resulting H&E stain provided adequate detail to identify monocytes and macrophages.

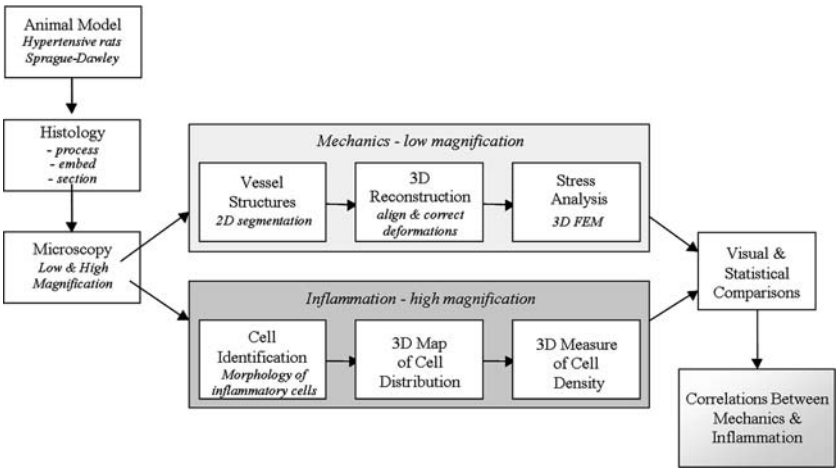


**Fig. 1** Flowchart of the research methodology, showing the analysis of stress and the measurement of inflammatory cell density as parallel and independent tasks

## 2.3 Microscopy

Figure 2 shows an idealized representation of a cross section (octagon), illustrating the size of a bifurcation relative to the section and the four registration holes. Bifurcations were identified by inspection of serial sections at low magnification on a Nikon Eclipse E800 microscope. A linearly encoded motorized stage (Ludl) was used to determine the location of the area of interest relative to the registration holes and to facilitate the creation of montages. A color CCD camera (Q-Imaging Micropublisher 5,459, 2,560 × 1,920 pixels) with a 20× objective (Nikon CFI Plan Apo 20×/0.75) was used to capture the necessary details to identify cells (0.167 μm/pixel). The size of the montages posed a significant challenge since the composite images consisted of large arrays of images. A 4× objective provided a sufficient field of view to capture all the structural information in a single frame. The resulting image resolution of 0.840 μm/pixel provided more than enough detail to identify vessel structures.

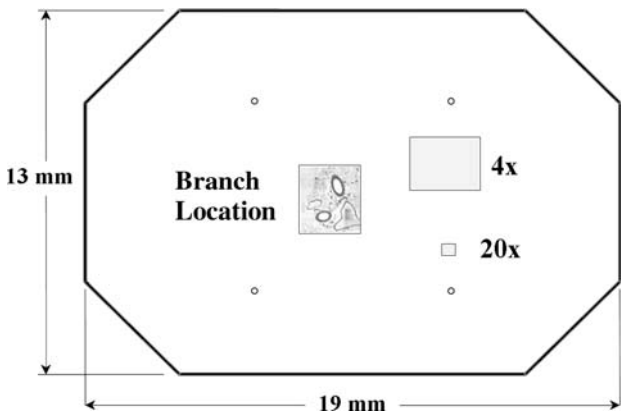


**Fig. 2** Schematic of a histological section (*octagon*) showing the location of a bifurcation, the array of registration holes and the fields of view with a 4× and a 20× objective

## 2.4 Segmentation

The red channel of the RGB images was used for segmentation because it provided the greatest contrast between the vessel wall and other structures in an H&E stained section. The features of interest are the inner boundary (chosen as the lumen) and the outer boundary (chosen as the external elastic lamina). The method of Perona and Malik (1990) was used to identify the vessel boundaries. The method uses the convolution of an image with a Gaussian kernel and a spatially varying anisotropic diffusion constant to keep the edges sharp while blurring the features away from the edges. Some manual intervention was needed to identify the outer boundary.

## 2.5 Deformation corrections

The hole positions on the face of the block were measured by mounting the block on a light microscope with an encoded motorized stage. Earlier work demonstrated that the holes were approximately straight and parallel to one another. Under these conditions, the distance between the holes does not vary significantly, especially over a short sectioning depth of about 1 mm. Therefore the hole positions on the block face were captured after sectioning and were assumed to remain constant through the sectioning depth. The deformed hole positions on individual sections were captured in a similar manner, but stage movement and image capture were automated after the first hole was identified. Because the GMA retained some eosin, the holes appeared white

on a light pink background and could be distinguished using thresholding.

An affine transformation was used to relate the hole positions before and after sectioning:

$$\begin{Bmatrix} x \\ y \end{Bmatrix} = \begin{bmatrix} c_1 & c_2 \\ c_4 & c_5 \end{bmatrix} \begin{Bmatrix} x' \\ y' \end{Bmatrix} + \begin{Bmatrix} c_3 \\ c_6 \end{Bmatrix}. \quad (1)$$

Here $x$ and $y$ are the undeformed hole coordinates, $x$' and $y$' are the deformed coordinates, and $c_1$ through $c_6$ are the six coefficients of the transformation. Four holes produce redundant data and a least squares approach was taken to minimize the error associated with a set of measurements. By extension of Eq. (1), the transformation becomes:

$$\begin{bmatrix} x'_1 & y'_1 & 1 & 0 & 0 & 0 \\ 0 & 0 & 0 & x'_1 & y'_1 & 1 \\ x'_2 & y'_2 & 1 & 0 & 0 & 0 \\ 0 & 0 & 0 & x'_2 & y'_2 & 1 \\ x'_3 & y'_3 & 1 & 0 & 0 & 0 \\ 0 & 0 & 0 & x'_3 & y'_3 & 1 \\ x'_4 & y'_4 & 1 & 0 & 0 & 0 \\ 0 & 0 & 0 & x'_4 & y'_4 & 1 \end{bmatrix} \begin{Bmatrix} c_1 \\ c_2 \\ c_3 \\ c_4 \\ c_5 \\ c_6 \end{Bmatrix} = \begin{Bmatrix} x_1 \\ y_1 \\ x_2 \\ y_2 \\ x_3 \\ y_3 \\ x_4 \\ y_4 \end{Bmatrix}. \quad (2)$$

From this equation, the coefficients of the transformation can be determined and the Cauchy strains calculated:

$$\varepsilon_x \cong c_1 - 1, \quad (3)$$

$$\varepsilon_y \cong c_5 - 1, \quad (4)$$

$$\varepsilon_{xy} \cong (c_2 + c_4)/2. \quad (5)$$

Figure 3 shows the mean strain results for a representative set of 56 sections. The mean extensional strain in the $x$-direction was 0.117 (±0.0017), while the mean extensional strain in the $y$-direction was 0.129 (±0.0024). The difference in the mean values indicates some anisotropy associated with sectioning, while the small standard deviations show the low section-to-section variability. The $y$-direction roughly corresponds with the cutting direction and produces somewhat larger positive strains, a consistent pattern for all the cases studied. But gross inspection of sections on the microtome indicated that they were compressed in the cutting direction before being placed on the water bath. The deformations produced during cutting may make the sections preferentially more compliant in this direction. Consequently, when the sections are floated on a water bath, they expand more in the cutting direction. The mean shear strain was −0.0013, which was within a standard deviation (±0.0016) of zero and was therefore neglected. Because the distortion pattern had a small standard deviation, the mean extensional strains in the $x$ and $y$ direction were used to correct the entire image stack.

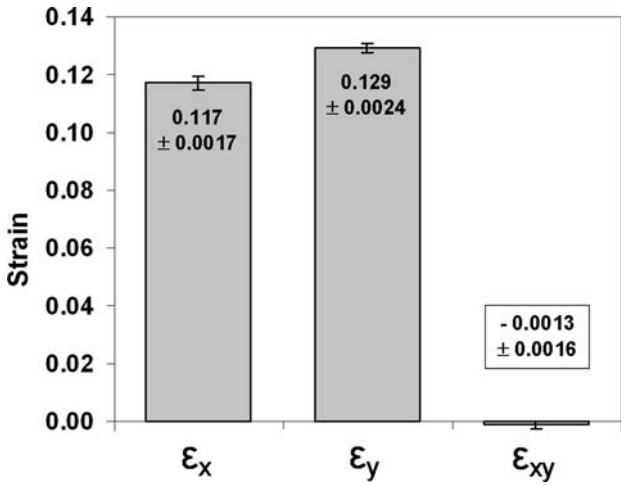


**Fig. 3** Mean strain components for all 56 sections from a representative case. The $x$-axis is perpendicular and the $y$-axis is parallel to the cutting direction

The registration holes produced a random error in alignment that was influenced by the estimate of the hole centroid positions on deformed sections and the relatively large distances between the holes and the region of interest (see Fig. 2). The registration holes were used to correct for deformations and alignment was improved by using an image similarity measure as described below.

## 2.6 Section alignment

An image similarity measure (ISM) was used to align serial sections, which have no common frame of reference. The strategy is to displace and rotate one image over the other until the overall image similarity is maximized. The mean square difference (MSD) between images (Studholme et al. 1997) was used as an inverse measure of image similarity:

$$\mathrm{MSD} = \frac{1}{N} \sum_{x,y \in X} \left[ I_2(x,y) - I_1(x,y) \right]^2. \quad (6)$$

$N$ represents the number of pixels over coordinate space $X$, while $I_1$ and $I_2$ represent serial images. The most rapid alignment was achieved by first coarsely aligning the images visually and then using a gradient descent method to converge to a position where the MSD was a minimum (Press et al. 1992).

For the MSD to accurately drive histological alignment, the serial images must be sufficiently close to one another to share common features. When reconstructing small arteries, it is desirable to use structures besides wall edges, such as cellular details, extracellular matrix (ECM) components and even other small vessels. In the mesentery tissue, adipose cells are prevalent, and

the walls of these cells are features that may be shared between serial sections. If a greater section interval is used (e.g. 50 μm), the vessel wall drives the alignment. Hence an artery that actually moved at an oblique angle relative to the sectioning plane would be erroneously represented by a more vertically aligned column. Poor alignment at large section intervals was confirmed by large changes in position of the registration holes from section to section. With some experimentation, a 10-μm interval was found to provide adequate shared detail for alignment.

### 2.7 Surface reconstruction

Using the segmentation techniques described, the inner and outer edges of the wall were identified in each section. The edges were reduced to point data that was compiled into two separate point clouds representing the inner and outer boundaries of the bifurcation. After preprocessing, a surface was created by using weighted alpha shapes to identify the intrinsic shape underlying the point data and to control the local detail (Edelsbrunner and Mucke 1994). Edelsbrunner and Fu (1998, 2002) have developed the program Geomagic Studio (Raindrop Geomagic, Inc.) that includes an efficient implementation of this approach with additional enhancements. Geomagic Studio can also create a non-uniform rational b-spline surface that exhibits better continuity between sections and can be readily imported into Ansys 7.0 (Ansys, Inc.) for finite element analysis.

Once the serial sections are aligned and deformations are corrected, the biological data from histology may be overlaid on the reconstruction. Hence, any biological markers that can be identified on GMA resin sections can be compared and correlated with the mechanical environment.

### 2.8 Midplane geometry and wall thickness

To simplify the mechanical analysis, the bifurcations are represented by elements at the midplane surface. Variable thickness shell elements can then be used in the finite element model, rather than solid elements. Shell elements can capture large variations in stress through the wall and require substantially less computational time than solid elements.

Matlab code (Matlab 7.0, MathWorks Inc.) was created to generate a midplane variable thickness model. The midplane and local thicknesses were defined by projecting a normal vector from the inner surface to its intersection with the outer surface. A ray tracing algorithm (Badouel 1990; Moller and Trumbore 1997) was implemented to determine the intersections between the normal of each inner polygon and the outer polygonal surface. The efficiency of this process is enhanced by describing possible intersections with barycentric coordinates. The midplane surface definition was only minimally affected if the outer normals were projected to intersect the inner surface instead of vice versa.

### 2.9 Reconstruction validation

Validating the reconstruction of small arterial bifurcations presents a challenge since the geometry is not known a priori. In addition, the histology-based methods described in this research are destructive and do not afford a second independent way to determine geometry. The reconstruction technique was validated by simulating microtomy of an idealized model of known geometry, reconstructing the model and evaluating the magnitude of the error. The idealized model was a detailed, well-defined surface that contained all the basic features of a small arterial bifurcation.

Microtomy was simulated by determining the intersection of this standard model with a series of evenly spaced parallel planes. The boundary contours were reduced to a point cloud and then reconstituted into a surface. After the reconstruction, the resulting model was compared to the original model and Fig. 4 shows the error for a reconstruction based on 13 transverse cross sections. Differences are shown as a color-coded map overlaid on the original model. The distances are measured from the original geometry with positive tolerances indicating that the reconstruction is outside the original geometry. While the distance scale for Fig. 4 is ±2.5 μm, over 90% of the surface area was within a narrower tolerance of ±0.5 μm. Given the size of the model, this tolerance translates to an error of less than 0.5% in position and about 1% of the smallest diameter. The localized fluctuations in the reconstructed geometry reflect the discretization of the surface into cross-sectional images of limited resolution. Greater accuracy in reconstructing a known geometry was achieved when the standard model was sectioned transverse to the longitudinal axis of the major vessel, as indicated in Fig. 4. Reasonably accurate reconstructions could be achieved with sections separated by 30 μm, as shown. The accuracy can be improved by reducing the section thickness and by increasing the resolution of images representing each section.

A reconstruction was also produced using nonlinear interpolation to generate intermediate images followed by surface creation using the marching cubes algorithm (Lorensen and Cline 1987). Figure 5 shows an example of a voxel-based reconstruction on the same sections used to simulate histology. Constraining points to

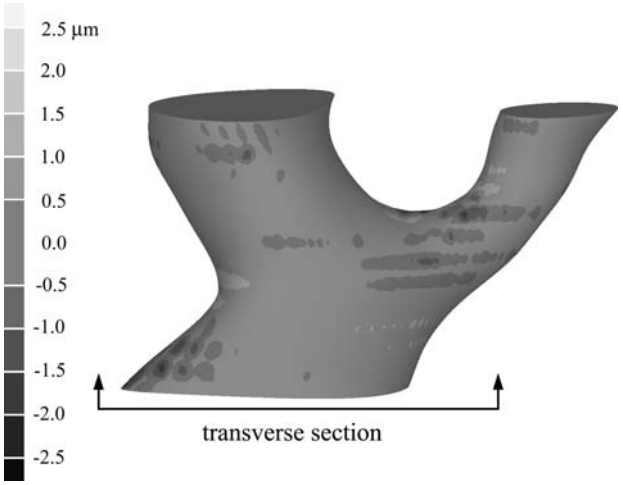


**Fig. 4** Accuracy of a point cloud reconstruction as compared to the original, idealized geometry. The reconstruction matches the original geometry within ±2.5 µm, with most of the surface exhibiting much smaller errors

discrete voxel locations produced ridges in the model. There is also a locally flattened region in the saddle of the bifurcation. This is due to the limited number of sections in the depth dimension and reflects some analytical difficulty in accurately capturing this saddle geometry using interpolation. Since stresses tend to be high in the saddle region, such flattening artifacts may significantly increase the local stresses. This highlights a key attribute of a point cloud-based reconstruction. With appropriate preprocessing, it is possible to more accurately capture such transitions, even if they occur in between image planes. The voxel-based reconstruction results in larger errors, driven by discretization error and interpolation problems in regions characterized by complex transitions in geometry.

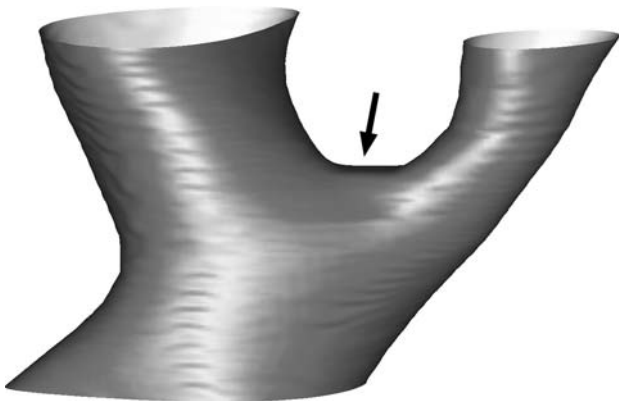

**Fig. 5** Polygonal surface produced by nonlinear interpolation and marching cubes surface creation for the idealized geometry. The *arrow* highlights a region where the surface is flattened due to artifact in the voxel-based reconstruction

### 2.10 Histology-based finite element model

A nonuniform rational b-spline surface was exported as an IGES file and imported into Ansys as a series of key points, lines and areas that could be meshed. The model boundaries were identified, extruded by about 50 µm away from the center of the bifurcation and fully constrained. After the analysis was completed, the extruded part of the model was deselected and not considered further. For the 7-day hypertensive bifurcation that we have used as a representative case, the core finite element model consisted of 3,344 variable thickness shell elements. Stress data in the upper and lower 10% of the model were not included in the spatial comparisons to further limit the influence of the constrained boundaries. A series of parametric studies showed that this approach provided good numerical stability, permitted the use of the complete reconstruction and reduced the high local stresses associated with constraining the model (Carnell 2004).

Ansys Shell Element Number 181 was used with nine integration points through the thickness. This element is suitable for analyzing moderately thick shell structures and accounts for changes in thickness and changes in loading caused by deformations.

Mechanical property measurements of mesenteric arteries were taken from the literature to form a homogeneous isotropic material model (Halpern et al. 1984; Ceiler and Mey 2000). Since the arteries were pressure fixed at 80 mmHg, the pressure applied to the finite element models is the incremental pressure increase above 80 mmHg. Therefore, the model stresses are incremental changes in stress from the pressure-fixed state. This approach emphasizes the changes in stress produced by cyclic loading, but does not accurately reflect the full magnitude of stresses produced by pressure. For hypertensive models, the incremental pressure increase was 100 mmHg (a total pressure of 180 mmHg). For normotensive models, the incremental pressure increase was 40 mmHg (a total pressure of 120 mmHg). Because pressure loads are incremental increases, the stress–strain relationship reflects the much stiffer incremental modulus of 2.0 MPa, and the stresses reported are actually changes in stress from the pressure-fixed state. Poisson's ratio was 0.49. The use of linear elastic material properties, pressure-fixed geometry and incremental changes in pressure affected the magnitude of stresses, but did not significantly alter the midplane stress distribution compared to a nonlinear hyperelastic model. Visual comparisons indicated that the linear and hyperelastic stress distributions at the midplane were very similar. Statistically, a Spearman rank correlation indicated an extremely high correlation in the stress distributions

($r_s$ = 0.930 and $Z_s$ = 54.3). While the hyperelastic material model was based on a curve fit of the same pressure–diameter data, it yielded somewhat lower midplane strains than the linear material model. For the 7-day hypertensive case highlighted, the average maximum principal strain was 0.137 for the linear material model and 0.117 for the hyperelastic material model. These comparisons suggest that the choice of material model does not substantially change the distribution or magnitude of stresses. The differences between the material models become more pronounced when considering stress variation through the wall or when considering geometry that is not pressure fixed.

### 2.11 Cell identification

Monocytes and macrophages were identified by their gross morphological appearance. A single observer, blinded to the treatment used, counted all macrophages. In addition, the fact that sections were not aligned and were viewed at high magnification prevented the observer from determining the geometry of the bifurcation as the cells were identified. Cell identification was done at a 20-μm interval to avoid identifying the same cell on multiple sections.

Histological characteristics used to identify monocytes and macrophages were their large size (~15 μm in diameter), their U-shaped nucleus and their characteristic blue cytoplasm. Mature macrophages contain secretory granules and a less characteristic nuclear shape. These cells also tend to be somewhat larger. Other cell types present in these sections (fibroblast, adipocytes, vascular smooth muscle cells, endothelial cells and lymphocytes) are structurally distinct.

To facilitate the identification of monocytes and macrophages, a graphic user interface (GUI) was designed. This GUI allowed an observer to zoom in and scroll through the montages at high magnification and identify various cell types based on morphology. The cell locations were noted in image space and later assembled into a three-dimensional point cloud of monocytes and macrophages. Monocytes and macrophages were presented collectively as a single cell density indicative of inflammation. A limited number of mast cells were separately identified, although this data will not be presented.

### 2.12 Quantifying inflammatory cell density

The distribution of cells was quantified using a sphere with a 150-μm radius for a series of local cell density calculations. The volume of lumen within each sphere was excluded from consideration since no inflammatory cells are present in this region. Also, the volume available for cells was reduced near the boundaries of the model space, so that cell density in these regions was not underestimated. The spherical subvolumes were centered on each cell or on each vertex of the luminal surface, as shown in Fig. 6. As the figure suggests, the cells themselves do not need to be visualized to describe cell density with respect to the bifurcation. Expressing cell density on the luminal surface also facilitated comparisons between cell density and mechanical stresses, since both were quantified at the same spatial location.

The size of the sphere used for cell density calculations, while somewhat arbitrary, did not affect the general pattern of inflammation within a range of values. However, there were practical considerations that limited the range of radii suitable for measuring local cell density. A much smaller radius (e.g. 50-μm) would largely exclude cells in the periadventitia. This would result in a mottled pattern of highs and lows dictated

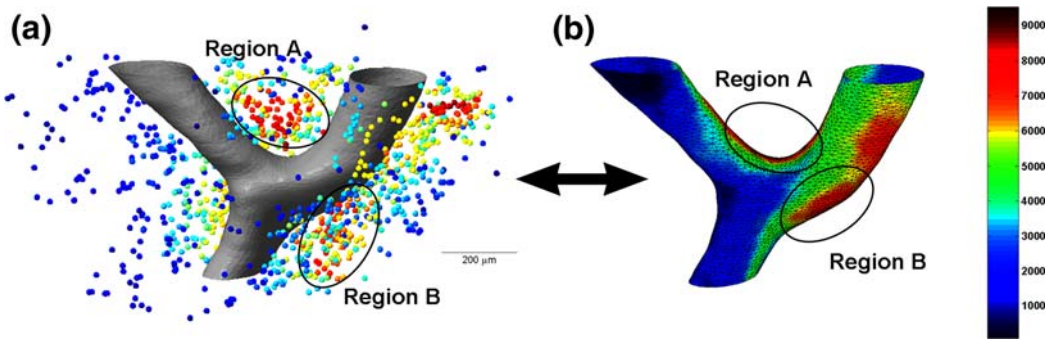


**Fig. 6** Combined monocyte and macrophage density (cells/mm$^3$) is represented by two methods, as shown for this 21-day hypertensive case. Density is calculated within 150 μm radius spheres **(a)** centered on each cell location and **(b)** centered on each vertex on the luminal surface. Regions A and B show that concentrations of cells captured by both methods. The surface representation is more directly comparable to stresses and avoids the difficulty of trying to visually determine three-dimensional distances between cells and the bifurcation

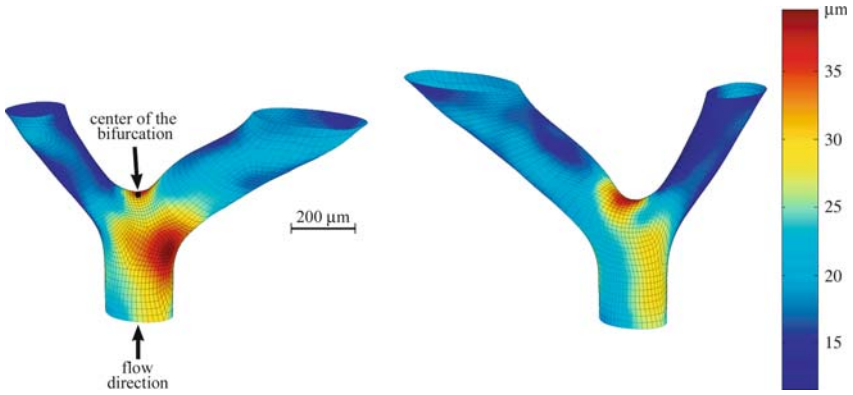


**Fig. 7** *Front* and *back* views of the luminal surface of a representative bifurcation harvested after seven days of hypertension. The *color coding* indicates wall thickness (μm). The direction of flow is indicated as is the center of the bifurcation, which is used to evaluate whether wall thickness is elevated in proximity to branching

by the precise positions of individual cells. A much larger spherical radius (e.g. 300-μm) spans the diameter of most of the vessels studied and would result in a more broadly averaged measure of cell density. A 150-μm radius avoided both the noise associated with much smaller subvolumes and the excessive blending associated with much larger subvolumes.

### 2.13 Comparing stress, wall thickness and inflammation

Because geometry varied greatly between bifurcations, most of the comparisons were focused on spatially comparing different characteristics within a given bifurcation. Von Mises stress at the midsurface was used because the stress gradients can be large and complex near bifurcations. Further, the definition of stress components and their interpretation can be difficult in the saddle region where an artery branches. The use of an invariant midplane stress avoids the added complexity of interpreting spatial and directional changes in component stresses. The distribution of wall thickness was also considered because it affects the stresses and wall thickening may indicate an inflammatory change.

Although side-by-side comparisons of stress, wall thickness and monocyte/macrophage density can provide useful insights, statistical methods are needed to rigorously identify trends and test hypotheses. Analysis showed that the data does not exhibit a normal distribution, underscoring the need to use a nonparametric statistical approach.

The Spearman rank correlation was used to compare characteristics of bifurcations. This nonparametric approach involves ranking both variables and then using these rankings as a distribution-free substitute for the original values (Walpole and Myers 1993). The strength of the association between the rankings can be characterized by a standard normal score ($Z_s$), based on the Spearman rank correlation coefficient ($r_s$) and the sample size ($n$):

$$Z_s = r_s\sqrt{n-1}. \tag{7}$$

The proximity to branching is assessed by first calculating the distance from each surface point to the center of the bifurcation. The center of the bifurcation is defined as the intersection of the axis of the mother vessel with the "flow divider" part of the bifurcation (see Fig. 7). This distance is an inverse measure of proximity and can be paired with any other arterial characteristic to determine if the characteristic is elevated near the center of the bifurcation.

Because of the unique characteristics of each bifurcation, it is difficult to rigorously compare the results from case to case. Hence, in addition to the visual and statistical comparisons within a bifurcation, the stress and cell density results were averaged for each bifurcation.

## 3 Results

### 3.1 Surface reconstruction and wall thickness distribution

Figure 7 shows the reconstruction of a representative bifurcation from a rat subjected to a 7-day exposure to Angiotensin II. The color-coded map in Fig. 7 indicates wall thickness in micrometers and shows high variability, especially in proximity to branching. Two localized peaks occur near the center of the bifurcation, where the principal radii of curvature are on opposite sides of the wall (i.e., in the saddle-shaped regions where the Gaussian curvature is negative). This condition may be viewed as a localized flattened region where the wall tension must be high to resist internal pressure (Harvey 1974). Similar patterns were evident among the other 7-day hypertensive cases and the 21-day hypertensive case, but not evident in the two normotensive cases. The mean wall thickness for the bifurcation in Fig. 7 was 21.8 μm and the standard deviation was 6.2 μm, which is 28.0% of the mean thickness. The four 7-day

hypertensive cases on average had a standard deviation in thickness that was 23.2% of the mean. This is considerably greater than the 12.3% deviation in thickness for the two normotensive cases, suggesting that medial thickening is more focal than uniform for a bifurcation. The 21-day hypertensive case had an 18.1% deviation in thickness.

### 3.2 Stress distribution

Figure 8 shows the von Mises stress distribution in kilopascals for a bifurcation after 7 days of hypertension. The greatest stress is in the central region shaped like a saddle, as indicated by an arrow in the left hand view. Secondary peaks can be seen in Fig. 8, as indicated by the arrows. These peaks are located in a saddle region before the point of flow division. Despite the greater thickness in regions where curvature might produce high stress, local stress peaks are still present. Similar peaks were evident for most of the 7-day hypertensive cases and the 21-day hypertensive case, but no consistent pattern was evident for the normotensive cases. Based on statistical comparisons, four of the five hypertensive cases and one of the two normotensive cases exhibited higher stresses in proximity to branching.

### 3.3 Cell density distribution

Figure 9a shows the monocyte/macrophage density coded to the individual cells for the 7-day hypertensive bifurcation. Generally, greater concentrations of cells occurred in the adventitial and periadventitial regions. The greatest cell density for the bifurcation in Fig. 9 was about 7,200 cells/mm$^3$, located in the periadventitial region distal to the point of flow division. All of the hypertensive cases exhibited greater cell density near the center of the bifurcation. Many of the local peaks in cell density occurred where complex curvature might produce high stresses. Regions A and B in Fig. 6 are two such examples for the 21-day hypertensive bifurcation. The normotensive cases did not exhibit a consistent cell density pattern in proximity to the center of the bifurcation.

Increased inflammatory cell density in proximity to branching corresponds with the trend of increased intramural stresses in proximity to branching. These findings suggest a direct correspondence between intra-

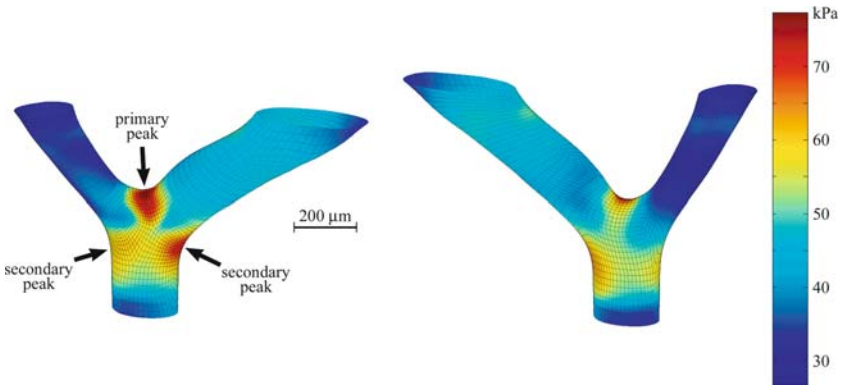


**Fig. 8** *Front* and *back* view of von Mises stress distribution in kPa for a bifurcation after seven days of hypertension

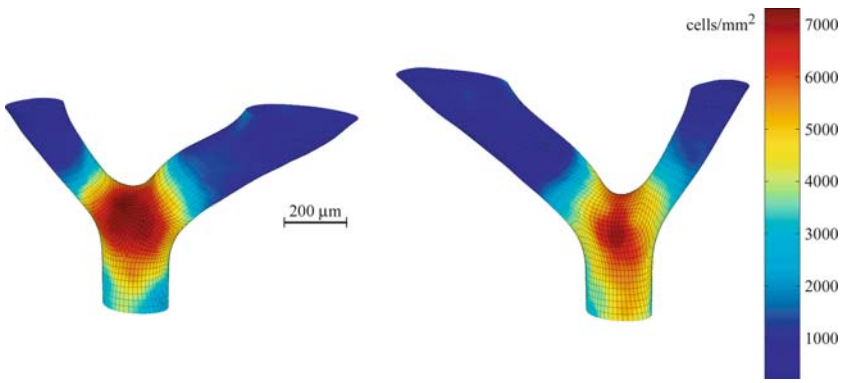


**Fig. 9** *Front* and *back* view of combined monocyte and macrophage density after seven days of hypertension (cells/mm$^3$)

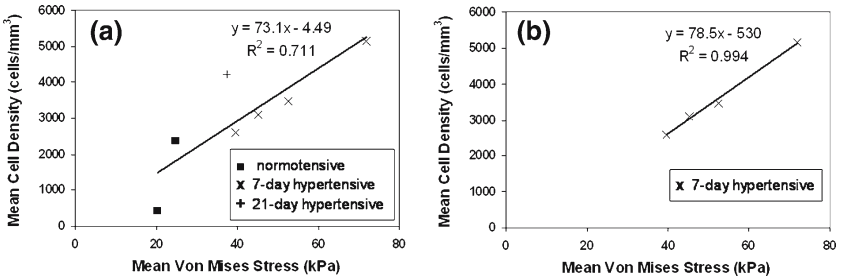


**Fig. 10** Mean cell density versus mean von Mises stress is shown **a** for all seven bifurcations and **b** for the four 7-day hypertensive bifurcations. Increased mean stress is associated with increased inflammation as measured by mean monocyte/macrophage density

mural stress and inflammation as measured by monocyte/macrophage density.

### 3.4 Comparisons of stress, wall thickness and inflammation

Visual observations suggest that stress, wall thickness and inflammation are all elevated near the center of bifurcations and that the peaks in stress and inflammation roughly correspond to one another. These characteristics were more rigorously compared by a series of Spearman rank correlations. Of particular interest was whether intramural stress, cell density or wall thickness were elevated near the center of each bifurcation, and whether stress was correlated to cell density.

For the 7-day hypertensive bifurcation in Fig. 7, wall thickness was shown to decrease moving away from the center of the bifurcation. This is not surprising since the wall thickness is expected to be greater in branching regions where the geometry might produce elevated stress. Using the Spearman rank correlation, the standard normal score for this trend is 12.8 indicating a high confidence level in the correlation ($p$ value $<0.001$). For all hypertensive cases, wall thickness is greater in proximity to branching. By contrast, wall thickness is lower in proximity to branching for both normotensive cases.

Von Mises stress was also statistically shown to be elevated in proximity to branching for the 7-day hypertensive case shown in Fig. 8. The standard normal score for the Spearman rank correlation was $-32.7$ ($p < 0.001$). Four of the five hypertensive samples exhibited this trend with an unusual pattern of stress seen for the bifurcation that did not follow the trend. The pattern was unclear between the two normotensive bifurcations, with one exhibiting a similar trend to the hypertensive cases and the other showing no significant trend.

The Spearman rank correlation between cell density and distance from the center of the bifurcation showed a strong correlation for the representative 7-day hypertensive bifurcation. In fact, all five hypertensive bifurcations showed that cell density was elevated in proximity to branching. This trend is consistent with the branching region being a focal point for remodeling during the onset of hypertension. The pattern was less clear among the normotensive bifurcations with one case exhibiting a positive correlation between cell density and the proximity to branching and the other exhibiting a weakly negative correlation.

The fact that intramural stress and inflammatory cell density are both elevated where branching occurs suggests they are related phenomena. To further evaluate the connection between these phenomena, we considered whether the regions of high intramural stress are spatially collocated with the regions of inflammation (as measured by monocyte/macrophage density).

The representative 7-day hypertensive bifurcation exhibited a strong correlation between von Mises stress and cell density. However, the Spearman rank correlations did not reveal a consistent pattern among all the hypertensive cases. A positive correlation was seen among three of the five hypertensive cases, a negative correlation for one case, and no correlation for the remaining case. The normotensive cases exhibited no correlation between stress and cell density.

Figure 10a shows the general trend between mean intramural stress and mean inflammatory cell density for all the bifurcations studied. The trend among all the cases indicates that greater mean stress is associated with greater mean inflammation, although the $R$-squared value is 0.71. As Fig. 10b indicates, the relationship between mean stress and inflammation is more strongly demonstrated by considering the four bifurcations from 7-day hypertensive rats. The slope of the trend line for the 7-day hypertensive cases is greater and the $R$-squared value is considerably higher at 0.99.

## 4 Discussion of methods

In this section, we discuss how geometric variability influenced the methods used to compare and interpret results. We also discuss the reconstruction method, our

use of a simplified constitutive model and our approach to quantifying cell density.

Geometric characteristics such as branch angle and the relative size of mother and daughter vessels varied considerably among the mesenteric bifurcations. Wall thickness and curvature also varied greatly within each bifurcation. The variability in wall thickness and curvature underscores the value of a histology-based approach, since such variations would be difficult to capture in an idealized geometric model (Thubrikar et al. 1990; Salazar et al. 1995). But such differences made it difficult to directly compare the bifurcations to one another. Presenting the detailed characteristics of each bifurcation leads to anecdotal observations, shifting the focus away from the broader trends. It was because of these challenges that we examined stress and inflammation within each bifurcation in detail, but limited our comparisons between bifurcations to averaged quantities and other more general observations.

One advantage of reconstructing geometry from a point cloud rather than using a voxel-based approach is that boundary data from multiple sections can be better integrated to generate a surface. Most voxel-based approaches use interpolation to generate intermediate images based on the images nearby. This interpolation tends to be computationally expensive because image intensities at each pixel location are used to generate the intermediate image. Substantial down-sampling is needed to use a voxel-based approach with the images in this research, resulting in a significant loss in spatial resolution and an unnecessary compromise in the precision of the final reconstruction. For this research, the loss of gray-level data does not affect the reconstruction, since the inner and outer surfaces are all that are needed. In fact, separating segmentation from reconstruction preserves the high spatial resolution of the boundaries from microscopy without carrying along the rest of the cross-sectional information through interpolation and surface creation. The disadvantage of a point cloud reconstruction is that adjusting segmentation is more difficult and time-consuming since the intensity data is discarded earlier in the process. If the surface features of interest are well defined, as they are in microscopy, the inability to carry intensity data further through the process is a worthwhile trade-off for the increased spatial resolution.

The use of pressure–diameter data from tubular segments to model the material behavior of a bifurcation introduces uncertainty in the stress results. The content and organization of the wall may be considerably different near bifurcations compared to tubular sections (Finlay et al. 1998; Liu 1998). Also, medial thickening generally reduces intramural stress but smooth muscle cell hypertrophy may produce thickening without a commensurate increase in rigidity.

Even without adaptive changes, bifurcations are unlikely to be homogeneous or isotropic and this is a limitation of the current study. It is certainly possible to assume a pattern of material property variation through each bifurcation, but given the current understanding of material properties within mesenteric bifurcations, such an assumption is likely to impose an artifact on the stress distribution. A detailed histology-based approach could account for patterns in the ECM organization. Efforts are underway to characterize ECM organization in two dimensions, but this more comprehensive approach is beyond the scope of the current study.

Although linear material properties were used to represent the incremental change in stress between the pressure-fixed state and systole, a five-parameter Mooney Rivlin hyperelastic model was also considered. Details and some comparative data were provided earlier, and the results indicated that the hyperelastic models substantially increased computation time without significantly changing the stress distributions at the midplane.

Immunostaining or in situ hybridization can be tied explicitly to cellular activity, but these techniques were not technically feasible. GMA is ideal for preserving soft tissue morphology, but the presence of GMA during staining can cause steric interference that artificially limits immunological binding. This is particularly problematic when a quantitative and repeatable approach must be applied to a series of sections. The gross characteristics of monocytes and macrophages are quite distinct. Simple staining is typically used to identify these cells in diagnostic clinical settings. Such a methodology, while time-consuming, avoids the problems with consistency and repeatability associated with immunological stains. Some error is associated with identifying individual cells, but we found good consistency in the 2D distributions of cells on adjacent sections. In addition, each sample in this study combines structural and cellular results from 40 to 60 histological sections. This integrated approach reduces uncertainty and variability associated with individual measurements.

As Fig. 6a shows, it is difficult to grasp the three-dimensional arrangement of cells around the bifurcation from any single point of view. Mapping the cell density to the luminal surface, as shown in Fig. 6b, eliminates the need to visualize the cells and facilitates the comparison of cell density with the intramural stress distribution. As a comparison of Fig. 6a and b suggests, a surface map can effectively convey the three-dimensional distribution of inflammatory cells.

## 5 Discussion of results

Figure 9 shows the combined monocyte and macrophage density for the representative 7-day hypertensive bifurcation. There is one primary peak in cell density that occurs in the region that we have defined as the center of the bifurcation. As previously discussed, this is the region where curvature characteristics heighten intramural stresses caused by arterial pressure. Note that the 21-day case shown in Fig. 6 also exhibits concentrations of inflammatory cells in these saddle-shaped regions. In fact, all five hypertensive bifurcations exhibited localized concentrations of monocytes/macrophages within these regions. Increased von Mises stress is positively correlated with increased cell density for three of the five hypertensive cases. In the absence of greater wall thickness in these regions, all five hypertensive bifurcations would include collocated peaks in intramural stress and inflammatory cell density.

The adaptive changes associated with the onset of hypertension appear to preferentially affect the transition geometry that is unique to bifurcations. It is reasonable to assume that the geometry of a bifurcation is already optimized before hypertension is induced, but remodeling is necessary after the onset of hypertension. More collagen may be present where stresses are greater or less uniform; an arrangement better suited to bear the existing loads, but less readily adapted to changes in loading. By this reasoning, the high wall thickness exhibited in hypertensive bifurcations may be an adaptive response to normalize the levels of intramural stress.

Based on the limited number of cases studied, both intramural stress and cell density are greater near bifurcations after the onset of hypertension. Also cell density peaks tend to occur where surface curvature would suggest a high intramural stress due to pressure. Further, the mean stress and mean cell density from each bifurcation exhibit a positive correlation (see Fig. 10). These findings collectively suggest that stress may stimulate inflammatory changes. However, the point-by-point comparison of stress and cell density within each bifurcation did not exhibit a consistent pattern. Among the five hypertensive cases, three cases showed a strong positive correlation between stress and inflammation, one case showed a strong negative correlation and one case showed no correlation. There are several possible reasons why this most stringent test was not conclusive. The hypothesized stimulus and response are measured at the same time but, in reality, the peak stimulus precedes the peak response. It is likely that adaptive changes in wall thickness and organization have occurred to reduce the initial stresses that may have stimulated macrophage recruitment. It is also possible that inflammatory cells are concentrated near but not coincident with the signaling mechanisms that stimulate recruitment. This would explain why a variety of findings suggest a correlation between intramural stress and inflammation without the point-by-point comparisons within each bifurcation corroborating the trend.

These observations are based on a limited number of samples and confidence in these results could be strengthened by expanding the study. A larger number of samples or additional time points might yield a more consistent pattern in the point-by-point comparisons of stress and inflammation.

The consideration of additional factors might also reveal a stronger connection between the mechanical environment and inflammation. As previously mentioned, a constitutive model accounting for variations in ECM content near bifurcations might more accurately predict stresses and potentially lead to stronger positive correlations. Also, elevated intramural stress is only one stimulus of inflammatory changes and other factors that were not studied may have influenced the pattern of inflammation. For example, endothelial dysfunction caused by wall shear stress may play an important role even during the onset of hypertension. Younis et al. (2004) found peaks in fluid and solid mechanical stresses in the human carotid bifurcation that corresponded with sites of early atherosclerotic inflammation. While our focus is on hypertensive changes, it is reasonable to infer that wall shear stress may also influence the pattern of inflammation caused by hypertension.

## 6 Conclusions

The reconstruction technique, finite element analysis, cell density characterization and visual and statistical comparisons collectively offer a methodology for other three-dimensional studies where mechanical and biological phenomena may be interrelated. Variability in branch angle, curvature and wall thickness make comparisons between bifurcations difficult. For the limited number of hypertensive bifurcations in this study, the point-by-point spatial comparison of stress and cell density did not consistently exhibit a positive correlation. The spatial and temporal differences that naturally occur between stimulus and response may make it unreasonable to expect a positive point-by-point spatial correlation. Peaks in intramural stress and monocyte/macrophage density occur near bifurcations after the onset of hypertension. The normotensive bifurcations showed lower levels of stress and inflammation and did not exhibit a consistent spatial correlation. Cell density peaks occur in regions where surface curva-

ture would create stress concentrations, independent of differences in wall thickness. Also, a strong positive correlation between mean stress and cell density in each bifurcation suggests they are related phenomena.

**Acknowledgments** We are grateful for the support of the National Institutes of Health (R01 HL-70531 and R01 HL-62820), the Woodruff School of Mechanical Engineering at Georgia Institute of Technology and the Cardiology Division of Emory University School of Medicine.

## References

AHA (2005) American Heart Association. Heart disease and stroke statistics—2005 update. American Heart Association, Dallas, Texas

Badouel D (1990) An efficient ray–polygon intersection. Graphics Gems

Capers Q, Alexander RW et al (1997) Monocyte chemoattractant protein-1 expression in aortic tissues of hypertensive rats. Hypertension 30:1397–1402

Carnell PH (2004) Intramural stress and inflammation in arterial branches: a histology-based approach. Woodruff School of Mechanical Engineering, Doctoral Dissertation, Georgia Institute of Technology

Ceiler DL, Mey JGRD (2000) Chronic NG-nitro-L-arginine methyl ester treatment does not prevent flow-induced remodeling in mesenteric feed arteries and arcading arterioles. Arterioscler Thromb Vasc Biol 20:2057–2063

Edelsbrunner H, Fu P (1998) Apparatus and method for geometric morphing. Raindrop Geomagic, Inc., USA

Edelsbrunner H, Fu P (2002) Methods of generating three-dimensional digital models of objects by wrapping point cloud data points. Raindrop Geomagic, Inc., USA

Edelsbrunner H, Mucke EP (1994) Three-dimensional alpha shapes. ACM Trans Graph 13(1):43–72

Finlay HM, Whittaker P et al (1998) Collagen organization in the branching region of human brain arteries. Stroke 29: 1595–1601

Fukui T, Ishizaka N et al (1997) p22phox mRNA expression and NADPH oxidase activity are increased in aortas from hypertensive rats. Circ Res 80:45–51

Glagov S, Bassiouny HS et al (1997) Mechanical determinants of plaque modeling, remodeling and disruption. Atherosclerosis 131(Suppl):S13–S14

Griendling KK, Alexander RW (1998) Cellular biology of blood vessels, Chap 4. In: Alexander RW, Schlant R, Fuster V (eds) The heart. McGraw-Hill, New York, pp 125–141

Halpern W, Osol G et al (1984) Mechanical behavior of pressurized in vitro prearteriolar vessels determined with a video system. Ann Biomed Eng 12:463–479

Harvey IF (1974) Theory and design of modern pressure vessels. Van Nostrand Reinhold, New York

Howard AB, Alexander RW et al (1997) Cyclic strain induces an oxidative stress in endothelial cells. Am J Physiol 272:C421–C427

Liu SQ (1998) Influence of tensile strain on smooth muscle cell orientation in rat blood vessels. J Biomech Eng 120(June 1998):313–320

Lorensen WE, Cline HE (1987) Marching cubes: a high resolution 3D surface construction algorithm. Comput Graph Q Rep SIGGRAPH-ACM 21(4):163–168

Moller T, Trumbore B (1997) Fast, minimum storage ray-traingle intersection. J Graph Tools 2(1):21–28

NHLBI (2003) National Heart, Lung, and Blood Institute. The Seventh Report of the Joint National Committee on Prevention, Detection, Evaluation, and Treatment of High Blood Pressure. C. A. V. Chobanian, National Heart, Lung, and Blood Institute

Ollerenshaw JD, Heagerty AM et al (1988) The effects of coarctation hypertension upon vascular inositol phospholipid hydrolysis in Wistar rats. J Hypertens 6:733–738

Perona P, Malik J (1990) Scale-space and edge detection using anisotropic diffusion. IEEE Trans Pattern Anal Mach Intell 12(7):629–639

Press WH, Flannery BP et al (1992) Numerical recipes in FORTRAN: the art of scientific computing. Cambridge University Press, Cambridge

Salazar RS, Thubrikar MJ et al (1995) Pressure-induced mechanical stress in the carotid artery bifurcation: a possible correlation to atherosclerosis. J Biomech 28(11):1333–1340

Studholme C, Hill DLG et al (1997) Automated three-dimensional registration of magnetic resonance and positron emission tomography brain images by multiresolution optimization of voxel similarity measures. Med Phys 24(1):25–35

Thubrikar MJ, Robicsek F (1995) Current review: pressure-induced arterial wall stress and atherosclerosis. Ann Thorac Surg 59:1594–1603

Thubrikar MJ, Roskelley SK et al (1990) Study of stress concentration in the walls of the bovine coronary arterial branch. J Biomech 23(1):15–26

Walpole RE, Myers RH (1993) Probability and statistics for engineers and scientists. Macmillan, New York

Willis GC (1954) Localizing factors in atherosclerosis. Can Med Assoc J 70(1):1–9

Wilson PW (1994) Established risk factors and coronary artery disease: the Framingham study. Am J Hypertens 7:7s–12s

Wolinsky H, Glagov S (1964) Structural basis for the static mechanical properties of the aortic media. Circ Res 14:400–413

Xu C, Zarins CK et al (2000) Differential transmural distribution of gene expression for collagen types I and III proximal to aortic coarctation in the rabbit. J Vasc Res 37(3):170–182

Younis HF, Kaazempur-Mofrad MR et al (2004) Hemodynamics and wall mechanics in human carotid bifurcation and its consequence for atherogenesis: investigation of inter-individual variation. Biomech Model Mechanobiol (3):17–32